

₁ This is a **non peer reviewed** pre-print uploaded to EarthArXiv
₂ The manuscript has been submitted to the Geophysical Prospecting and is cur-
₃ rently undergoing peer-review.

Shear-wave splitting measured for permanent reservoir monitoring systems: an example from the Snorre field

Joseph Asplet¹, J-Michael Kendall¹, Annie Jerkins², and Tom Kettlety¹

¹Department of Earth Sciences, University of Oxford, U.K.

²NORSAR, Kjeller, Norway

Friday 5th September, 2025

Abstract

Microseismic monitoring of offshore CO₂ storage projects is likely to include some deployment of offshore sensors. To improve the value proposition of this monitoring infrastructure, it is important to consider what other information can be gained about the CO₂ storage complex and the surrounding region. Shear-wave splitting is one potential source of added value to microseismic monitoring of CO₂ storage operations at minimal additional cost, if factored in during network design. Shear-wave splitting provides a means to passively monitor the *in situ* horizontal maximum stress azimuth and potentially the magnitude of differential horizontal stresses. We demonstrate this for offshore monitoring of reservoirs using data recorded by the permanent reservoir monitoring (PRM) network at the Snorre field. We measure shear-wave splitting for the M_W 5.1 Tampen Spur earthquake and subsequent microseismic aftershocks. Our results show that high-quality shear-wave splitting measurements can be made for microseismicity, with M_L ≥ 0.7, recorded by seafloor instruments. At Snorre, the average shear-wave splitting fast polarisation direction $\phi_f = 92 \pm 15^\circ$ and percentage anisotropy $\xi = 2.68 \pm 0.26$. This is consistent with microcracks preferentially aligned with the maximum horizontal stress azimuth. At Snorre we estimate this as $108 \pm 4^\circ$ using data from the World Stress Map. The shear-wave splitting results contain two groups of fast polarisation directions. The four westernmost stations cluster around $\phi_f = 68 \pm 13^\circ$ with the remaining clustering around $\phi_f = 113 \pm 4^\circ$. This variation may be due to the depletion history of the reservoir. Incorporating shear-wave splitting into microseismic monitoring plans potentially allows for semi-continuous measurements of the changes to the stress field in the storage complex and surrounding region, provided there is sufficient microseismicity. This demonstrates that shear-wave splitting is a valuable dataset for monitoring the offshore subsurface stress field, which should be considered when planning offshore passive seismic monitoring.

1 Introduction

Geological CO₂ storage is an essential part of global net zero strategies. Many countries including the UK, Norway, Denmark, and the Netherlands are developing offshore geological storage projects in the North Sea, as the geology is favourable for geological storage and there is existing infrastructure and technical expertise which can be redeployed (Furre et al., 2019; Skurtveit et al., 2022). With the growth in project development there is an increasing demand for new approaches to characterise the *in situ* stress state of prospective sites, and to monitor the geomechanical response of the storage complex to CO₂ injection. This is needed to ensure the safety and operability of CO₂ storage sites (Skurtveit et al., 2022).

One important component of monitoring geological carbon storage projects is seismicity. Fluid injection has been associated with seismicity in a wide range of geological settings (e.g., Keranen and Weingarten, 2018) including CO₂ injection (e.g., Stork et al., 2015; Harvey et al., 2021; Bauer et al., 2022) and offshore gas storage (Cesca et al., 2014). For the North Sea, a high quality seismicity catalogue has been compiled (Kettlety et al., 2024), enabling improved assessment of faulting, the background stress field, leakage risk, and seismic hazard for projects (Kühn et al., 2025). One recommendation from this body of work is that offshore seismic monitoring infrastructure is needed if seismicity near CO₂ storage projects is to be monitored with sufficient accuracy. Offshore (i.e., near-source) observations are vital in calculating accurate earthquake locations (particularly depths), focal mechanisms, and magnitudes.

Achieving a high quality catalogue of seismicity is the primary product for any passive seismic monitoring programme, to better understand how the reservoir is responding to injection. However, deploying networks of seismometers on the seafloor has the potential to generate highly valuable secondary datasets, further aiding that understanding, particularly if acquiring these secondary data products is incorporated into the network design. One such dataset is shear-wave splitting, which is an indicator of seismic velocity anisotropy – the variation in seismic velocity with propagation direction – measured using microseismicity. This can provide a measure of the *in situ* stress field. Fracture-induced seismic anisotropy has previously been observed using 4 component sea bottom cable systems at the Valhall field using P wave amplitude variation with offset and azimuth (AVOA, Hall and Kendall, 2003) and seismic interferometry (Mordret et al., 2013). Such seafloor instrumentation has

68 been previously used to monitor induced seismicity (Chambers et al., 2010)

69 1.1 Shear-wave splitting

70 Shear-wave splitting, or seismic birefringence, occurs when a shear-wave propagates
71 through an anisotropic medium. The incident shear-wave is split into two sub-
72 perpendicular shear-waves which propagate through the medium at different velocities
73 (Figure 1). The polarisation of the fast shear-wave (ϕ) and the delay time between
74 the split shear waves (δt) is measured where ϕ is related to the orientation of the
75 symmetry axes of the anisotropic medium and δt to the strength of the anisotropy.
76 Shear-wave splitting is typically measured using passive seismic data and has been
77 measured in many industrial settings using microseismic data (e.g., Al-Harrasi et al.,
78 2011b; Stork et al., 2015; Hudson et al., 2024, etc.,) including for offshore fields using
79 data from borehole geophones (Valhall; Teanby et al., 2004a) and ocean bottom
80 instruments (Ekofisk; Jones et al., 2014).

81 In the Earth there are many potential mechanisms for seismic anisotropy. At the
82 reservoir scale and depth the predominant mechanism is preferential alignment of
83 near-vertical micro-scale fractures with the azimuth of maximum horizontal stress
84 (S_{Hmax} ; Nur and Simmons, 1969; Crampin, 1987; Zatsepin and Crampin, 1997).
85 This mechanism produces a hexagonal anisotropy with a horizontal symmetry axis,
86 known as horizontal transverse isotropy (HTI). Sedimentary strata can also develop
87 anisotropy either through periodic layering of different units (e.g., Backus, 1962), or
88 preferred alignment of anisotropic minerals such as phyllosilicates (Kendall et al.,
89 2007). These mechanisms, however, produce a hexagonal anisotropy with a vertical
90 symmetry axis or vertical transverse isotropy (VTI). In passive seismic studies where
91 receivers are at the surface, the incident shear-waves are near vertical and, therefore,
92 are not sensitive to VTI. If data from borehole geophones are used, where ray-paths
93 are propagating horizontal from sources to receivers, then this contribution from
94 sedimentary fabrics, and the fact that the combination of VTI and HTI mechanisms
95 produces an anisotropy with an orthorhombic symmetry, must be considered but can
96 provide additional reservoir information (Baird et al., 2013). Where the observed
97 seismic anisotropy is due to the stress-induced alignment of micro-scale fractures, this
98 can be used to gain information on the *in-situ* stress field, particularly the orientation
99 of maximum horizontal stress (S_{Hmax}). S_{Hmax} is generally parallel to fracture strike
100 and, therefore, to the shear-wave splitting fast polarisation direction. This allows for
101 the orientation of S_{Hmax} to be interpreted from passive seismic shear-wave splitting

102 datasets (e.g., Savage et al., 2010; Igonin et al., 2022; Guzman et al., 2022; Hudson
103 et al., 2024). In some cases, it has been possible to infer changes in the stress state
104 at a reservoir using temporal variations in shear-wave splitting (e.g., Teanby et al.,
105 2004a; Stork et al., 2015) and in tectonic (e.g., Pastori et al., 2019) and volcanic
106 settings (e.g., Gerst and Savage, 2004; Kendall et al., 2025). The Ekofisk Microseismic
107 experiment, where microseismic data was acquired over an 18-day period in April
108 1997 at the Ekofisk oil field in the North Sea, showed that shear-wave splitting could
109 be used to illuminate spatial variations in aseismic fracture sets (Jones et al., 2014).

110 Whilst shear-wave splitting has been measured for microseismicity in offshore
111 settings, such as at Valhall (Teanby et al., 2004a) and Ekofisk (Jones et al., 2014),
112 this has relied on geophones installed in monitoring boreholes. Using sea floor instru-
113 mentation, such as ocean bottom seismometers or permanent reservoir monitoring
114 deployments, to measure shear-wave splitting has proved challenging given the in-
115 creased noise levels in the marine environment and uncertainty on sensor component
116 orientations. Where shear-wave splitting has been measured using seafloor instru-
117 ments it has often been for teleseismic shear-wave in deeper oceanic environments
118 (e.g., Harmon et al., 2004; Collins et al., 2012; Scholz et al., 2018). Shear-wave
119 splitting has been successfully measured for earthquakes with $M \geq 2.5$ using a
120 deployment of 150 ocean bottom seismometers over a subsea area of 300×1000 km
121 off the coast of northeastern Japan (S-net; Uchida et al., 2020).

122 The potential application to CO₂ storage is particularly exciting, since ensur-
123 ing safe and reliable geological CO₂ storage requires new methods to monitor the
124 geomechanical response of reservoirs to injection (Skurtveit et al., 2022). This is
125 because *in situ* stress state can naturally have a significant impact on the operation
126 and containment risk assessment of storage projects. Many potential CO₂ storage
127 sites require drilling and operating injection wells in regions or depths that may
128 not have had previous hydrocarbon exploration and, therefore, there may be fewer
129 data to conduct leakage risk assessments. Additional means of constraining stress
130 or fracturing are valuable, particularly when they are derived from independent
131 geophysical methods, to image the reservoir, seal, and overburden units. Fracture
132 and fault trends in particular are important inputs in containment risk assessment,
133 as their orientations with respect to *in situ* stresses significantly affect their potential
134 behaviour when stress changes occur as a result of injection. The likelihood of fault
135 failure, fracture development, and other deformation are affected by stress, and thus
136 it is a critical variable to constrain when assessing a field for CO₂ injection and

137 monitoring operations.

138 Understanding the *in situ* stress state can have a significant impact on the
139 operation and containment risk assessments of storage projects. Many potential CO₂
140 storage sites require drilling and operating injection wells in regions or depths that may
141 not have had previous hydrocarbon exploration and, therefore, there may be fewer
142 data to conduct leakage risk assessments. Additional means of constraining stress
143 or fracturing are valuable, particularly independent geophysical methods to image
144 the reservoir, seal, and overburden units. Fracture and fault trends in particular are
145 important inputs in containment risk assessment, as their orientations with respect to
146 *in situ* stresses significantly affect their potential behaviour when stress changes occur
147 as a result of injection. The likelihood of fault failure, fracture development, and
148 other deformation is affected by stress, and thus it is a critical variable to constrain
149 when assessing a field for CO₂ injection and monitoring operations.

150 2 Data

151 2.1 Permanent reservoir monitoring systems

152 Permanent reservoir monitoring (PRM) systems, consisting of three-component
153 geophones and hydrophones, have been deployed to monitor oil and gas fields in the
154 northern North Sea (Thompson et al., 2015). Similar PRM systems could be an
155 option for monitoring of offshore CO₂ storage fields, but shear-wave splitting is not
156 routinely measured for data recorded by these systems. PRM data for three fields in
157 the northern North Sea — Snorre, Grane and Oseberg — are good sites to test the
158 potential for PRM systems to measure shear-wave splitting. Data from select PRM
159 stations are shared with the Norwegian National Seismic Network (NNSN; Figure
160 3 Ottemöller et al., 2021). The PRM systems installed at the Snorre field is the
161 only one found to have suitable seismicity, using the unified North Sea earthquake
162 catalogue produced by the SHARP project (Kettlety et al., 2024; Kettlety et al.,
163 2025). The PRM system installed at Snorre is one of the largest in the world
164 (Thompson et al., 2015; Jerkins et al., 2024), consisting of a seismic cable containing
165 10,708 four component sensors, which have an eigenfrequency of 15 Hz.

166 Whether shear-wave splitting can be measured for an earthquake is limited by the
167 ‘shear-wave window’. Interactions with the free surface affect the particle motion of
168 shallow incident angle shear-waves (Nuttli, 1961). To avoid these effects, shear-wave
169 splitting is only measured where the incidence angle is less than the critical angle

(Booth and Crampin, 1985). We use a critical angle, or shear-wave window, of 45° for straight line ray paths between the source and receiver. This assumes that low velocity layers near the surface will turn incident shear-wave ray paths such that they are near-vertical at the free surface.

These events include the 21st March 2022 M_W 5.1 Tampen Spur earthquake and 26 subsequent aftershocks. The mainshock and five subsequent aftershocks are taken from the unified North Sea earthquake bulletin (Kettlety et al., 2024; Kettlety et al., 2025). This initial dataset is supplemented by additional aftershocks detected using the Snorre PRM system (Jerkins et al., 2024). The aftershocks have local magnitudes in the range $-0.6 < M_L < 2.6$. Waveform data for all earthquakes were obtained for the 10 PRM nodes shared with the NNSN and for the Tampen Spur mainshock data from an additional 50 PRM stations were provided by Equinor. An example of the data used, which includes horizontal component seismograms recorded by PRM stations within the shear-wave window of a M_L 0.7 aftershock, is shown in Figure 2.

2.2 Stress Data

Data from the 2025 release of the World Stress Map (Heidbach et al., 2025) are used to characterise the regional S_{Hmax} azimuth near the Snorre field (Figure 3). This dataset comprises 129 data points across the northern North Sea compiled from a variety of measurement types including: earthquake focal mechanisms (24 data points); borehole breakouts (58 data points); overcoring (5 data points); and drilling induced tensile fractures (24 data points). Data in the World Stress Map are assigned a data quality code based on their reliability to assess regional stress field orientation (Heidbach et al., 2016). Only data which are rated as A, B, or C on the World Stress Map data quality scheme are used, which gives a stress dataset comprising 50 measurements. The quality codes A, B, and C indicates the data has an uncertainty in S_{Hmax} orientation of $\pm 15^\circ$, $\pm 20^\circ$ or $\pm 25^\circ$ respectively.

3 Method

If a shear-wave has only propagated through isotropic media, and has a sufficiently vertical incidence angle such that phase shifts from interactions with the free surface can be neglected (Nuttli, 1961), the displacement recorded by a single seismometer can be written as:

$$\mathbf{u}(\omega) = u(\omega)\hat{\mathbf{p}} \quad (1)$$

201 in the frequency domain, where $u(\omega)$ is the source wavelet in the frequency domain
 202 and $\hat{\mathbf{p}}$ is the source polarisation. In this case the expected particle motion in the
 203 horizontal components is linear. If, however, the shear-wave propagates through
 204 anisotropic media, the delay time added by shear-wave splitting results in a phase
 205 shift which produces a characteristic elliptical particle motion. Therefore, shear-
 206 wave splitting can be effectively measured by searching for a set of shear-wave
 207 splitting parameters $(\phi, \delta t)$ which restore a linear particle motion. Here a method
 208 known as eigenvalue minimisation is used to characterise particle motion linearity
 209 (Silver and Chan, 1991; Walsh et al., 2013). For a shear-wave isolated in a time
 210 window of interest, where the optimum time window is found using cluster analysis
 211 (Teanby et al., 2004b), the horizontal component seismograms are rotated from the
 212 geographic to the radial-transverse reference frame, and the covariance matrix is
 213 computed following Walsh et al. (2013). The first and second eigenvalues, λ_1 and λ_2 ,
 214 correspond to the energy of the radial and transverse components respectively. Using
 215 the implementation of Wuestefeld et al. (2010) we grid search over the range of
 216 plausible shear-wave splitting parameters, $-90^\circ \leq \phi_f \leq 90^\circ$ and $0 \text{ s} \leq \delta t \leq 0.1 \text{ s}$,
 217 seeking to minimise $\frac{\lambda_2}{\lambda_1}$. Error estimates in $\phi_f, \delta t$ are made using a 95% confidence
 218 region defined by

$$\lambda_2(\phi_f, \delta t) \leq \lambda_{2_{min}} \{1 + [k/(v - k)] F_{k, v-k}^{0.05}\}, \quad (2)$$

219 where k is the number of parameters, in this case 2, v is the estimated degrees of
 220 freedom of the data, and $F_{k, v-k}$ is an F-distribution (Silver and Chan, 1991; Walsh
 221 et al., 2013). Standard errors in $\phi_f, \delta t$ are then estimated by taking the quarter of
 222 the length and width of the 95% uncertainty ellipsoid. Figure 4 shows an example
 223 shear-wave splitting measurement made for a M_L 0.7 aftershock of the Tampen Spur
 224 event. This example has a signal-to-noise ratio of 5.

225 The measured shear-wave splitting delay time, δt , is integrated along the entire
 226 ray path. Therefore, δt may vary with earthquake depth depending on the thickness
 227 of the anisotropic medium. To correct for ray path length effects δt is converted to
 228 percent anisotropy,

$$\xi = 100(V_S * \frac{\delta t}{d}), \quad (3)$$

229 where V_S is an assumed mean shear-wave velocity and d is the ray path length,
 230 assuming a straight ray from source to receiver.

4 Results

Shear-wave splitting measurements are made using waveform data for the Tampen Spur mainshock and subsequent aftershocks recorded by permanent reservoir monitoring stations at Snorre. After discounting stations that are outside of the shear-wave window for the earthquakes, we are able to make 124 shear-wave splitting measurements. After data quality control there are 25 good quality measurements of shear-wave splitting, with a further 28 clear null measurements where no shear-wave splitting is observed. Figure 5 shows the 25 good quality shear-wave splitting measurements at the recording station. The level of data attrition, with approximately 20% of measurements resulting in good quality splits is lower than other studies of microseismic shear-wave splitting (e.g., Teanby et al., 2004a; Pastori et al., 2019; Asplet et al., 2024; Asplet et al., 2025). One reason for the higher rate of data attrition is that few of the PRM sensors yield usable shear-wave splitting measurements for the Tampen Spur mainshock. This is due to the larger amplitude shear-waves either not being fully recorded due to data clipping, or the energetic wave trains cause significant ringing on the sensors. Both mean clear shear-wave splitting measurements cannot be made. Figure 6 shows the S-phase recorded by the closest line of 10 PRM sensors to the mainshock. No good quality shear-wave splitting measurements can be made for these data.

To estimate the regional S_{Hmax} azimuth at Snorre, we use data from the 2025 release of the World Stress Map (Heidbach et al., 2025). However, there are few datapoints close to Snorre, with the closest being 19 km from the centre of the PRM network. The regional S_{Hmax} azimuth is estimated by taking the circular mean of the 25 datapoints that are within 50 km of the centre of the PRM network. This gives a regional S_{Hmax} of $108 \pm 4^\circ$. This estimate of S_{Hmax} rotates to favour a near east-west S_{Hmax} azimuth as the radius of the averaging area increases (Figure 7).

The good quality shear-wave splitting measurements are concentrated to the North of the Snorre field (Figure 5). Seven measurements of shear-wave splitting are made for the Tampen Spur mainshock, with the remaining 18 made for the aftershocks. Of those, 11 are made for aftershocks with $M_L \leq 1.0$. Averaging the ϕ_f results from all the PRM sensors gives a circular mean ϕ_f of $-85 \pm 13^\circ$ (Figure 8). When aggregated the ϕ_f measurements show a slight bimodal distribution. This arises as the measured ϕ_f varies across the stations, with stations SNO01, SNO03, SNO05 and SNO08 measuring ϕ_f approximately oriented northeast-southwest (Figure 5,9a).

265 The 13 ϕ_f measurements made for data recorded by SNO01, SNO03, SNO05 and
 266 SNO08 (hereafter referred to as Group 1) have a circular mean of $\bar{\phi}_f = 68 \pm 13^\circ$ and
 267 the circular mean for the 12 ϕ_f measurements made at the remaining stations (or
 268 Group 2) $-67 \pm 4^\circ$ (Figure 9).

269 Shear-wave splitting delay times are converted to ξ following Equation 3. As all
 270 the earthquakes used here have focal depths in the range of 19.5 – 26.2 km (Jerkins
 271 et al., 2024), the measured δt are small relative to the ray path lengths with a
 272 mean ξ of 1.09 ± 0.08 , assuming a mean V_S of 5.7 km s^{-1} , calculated from a 1-D
 273 velocity model for the region (Jerkins et al., 2024). As we expect the majority of
 274 the anisotropy to be concentrated in the upper 5 km we also calculate ξ using this
 275 assumption, fixing the ray path length to 5 km and using an average V_S of 4.2 km s^{-1} .
 276 Under this assumption, the mean ξ is 2.68 ± 0.26 . Figure 10 shows histograms of ξ
 277 for all shear-wave splitting measurements.

278 5 Discussion

279 The results show that shear-wave splitting can be measured for microseismicity
 280 recorded by seafloor permanent reservoir monitoring systems. This demonstrates
 281 projects with nearby seafloor passive seismic sensors could use shear-wave splitting
 282 as a valuable tool for monitoring *in situ* $S_{H\max}$ azimuth at a higher spatial resolution
 283 than can be practicably achieved with stress data derived from borehole data. The
 284 percentage anisotropy results suggest that, as expected, the shear-wave splitting is
 285 mainly sensitive to anisotropy due to aligned microcrack in the upper crust. When
 286 we assume this region is 5 km thick, $\bar{\xi} = 2.68 \pm 0.26$, which is in line with what would
 287 be expected for anisotropy due to aligned microcracks in the uppermost crust (e.g.,
 288 Teanby et al., 2004a; Al-Harrasi et al., 2011a). The ϕ_f results show a clear bimodal
 289 pattern (Figure 8a). This is due to spatial variability in the data, with ϕ_f data for the
 290 Group 2 stations (circular mean $-67 \pm 4^\circ$, Figure 9b) strongly agreeing with regional
 291 $S_{H\max}$ azimuth ($108 \pm 4^\circ$; Figure 8b). The ϕ_f results for Group 1 form a second
 292 cluster rotated by 45° from the Group 1 results. This could represent a 45° rotation
 293 in the local $S_{H\max}$ azimuth at these southern and western stations. Similar scale local
 294 scale variations in ϕ_f have been observed by local studies of shear-wave splitting for
 295 microseismicity near a geothermal project and interpreted as local rotation of the
 296 $S_{H\max}$ azimuth (Hudson et al., 2024). Reservoir scale rotations of microscale fracture
 297 strike were observed for the Valhall field from amplitude variation with offset and

azimuth (AVOA Hall and Kendall, 2003) and seismic interferometry (Mordret et al., 2013). Spatial and temporal variations in shear-wave splitting were also observed using downhole microseismic monitoring, with reservoir scale rotations in ϕ_f of up to 90° (Teanby et al., 2004a). At Valhall the elliptical pattern in seismic anisotropy is associated with a radial S_{Hmax} azimuth tangential to a production related subsidence bowl (Hatchell et al., 2009; Herwanger and Horne, 2009; Mordret et al., 2013). The temporal variations in seismic anisotropy have been since been explained a cyclic recharge and dissipation of cap-rock stresses in response to production-driven compaction of the underlying oil reservoir (De Meersman et al., 2009).

One important difference between the data used in this study and anisotropy studied at Valhall is that the seismicity have depths in the range of 19.5 – 26.2 km (Jerkins et al., 2024), and that, therefore the shear-wave splitting and interpreted S_{Hmax} corresponds to the stress field averaged across the upper ca. 5 km of crust and not the state of stress within the Snorre field or overlying formations. Whilst the rotation in ϕ_f at Snorre may be associated with the depletion history of the reservoir, with the data available other explanations cannot be ruled out. One plausible alternate explanation is a more complicated anisotropic fabric, perhaps due to multiple cross cutting fracture sets (e.g., Al-Harrasi et al., 2011a; Verdon and Kendall, 2011). For this study it was only possible to use data from a handful of PRM stations at Snorre, and analysis data from all 10,708 PRM sensors would allow for more detailed analysis as to whether this rotation in ϕ_f represents a local rotation in S_{Hmax} across the area.

Shear-wave splitting has been previously measured using microseismicity at reservoir depths using both downhole (Teanby et al., 2004a) and seafloor instruments (e.g., Jones et al., 2014). Our results demonstrate that shear-wave splitting can also be routinely measured using naturally occurring microseismicity using offshore seafloor monitoring systems. Shear-wave splitting represents a valuable secondary dataset for a monitoring program, measured after microseismicity has been detected and located, which can be used passively infer the *in situ* stress field. Whilst deploying a PRM system at the same scale as that at Snorre may be unfeasible for typical CO₂ storage projects, the results for the 10 sensors shared with the NNSN (magenta triangles, Figure 5) yield a significant (15 out of 25) proportion of the shear-wave splitting dataset. Removing the 10 measurements made using an additional 50 sensors for the Tampen Spur mainshock does not change the interpretation of the results. This shows that even a minimal seafloor deployment could be used to measure microseismic

333 shear-wave splitting for stress field monitoring.

334 To maximise the value shear-wave splitting can add to a monitoring network it
335 is important to consider the limitations of the technique, particularly the spatial
336 limitations of the shear-wave window effect. For this study we are fortunate that
337 the 2022 Tampen Spur mainshock and subsequent aftershocks were sufficiently deep,
338 in the range of 19.5 – 26.2 km (Jerkins et al., 2024), and close to the Snorre field
339 that, with the exception of stations SNO7, SNO8 and SNO10, the PRM system was
340 within the shear-wave window of natural seismicity. This limits the impact on data
341 availability due to the shear-wave window effect (Nuttli, 1961). To make use of data
342 from potential induced microseismicity, which may have depths on the order of ca.
343 1 km depending on the depth of the reservoir, sensors would have to be more densely
344 spaced or placed closer to the microseismic events. The amount of good quality
345 shear-wave splitting measurements which could be made relative to the number
346 of measurements attempted is lower than for land based studies of microseismic
347 shear-wave splitting (e.g., Teanby et al., 2004b; Igonin et al., 2022; Asplet et al.,
348 2024; Asplet et al., 2025). This was expected as offshore sensors typically yield noisier
349 passive seismic data. Where measurements are made, the shear-wave waveforms are
350 clear and measurements can be made for multiple earthquakes with $M_L < 1.0$.

351 Presently, shear-wave splitting can be used to monitor S_{Hmax} azimuth using
352 microseismicity (e.g., Igonin et al., 2022; Hudson et al., 2024; Kühn et al., 2025;
353 Asplet et al., 2025) and to infer temporal variations in stress (e.g., Teanby et al.,
354 2004a; Stork et al., 2015). Further work should link models of stress-induced shear-
355 wave splitting, such as the anisotropic poroelasticity (APE) model of Zatsepin and
356 Crampin (1997), with geomechanical reservoir models. This would allow for the
357 adaptation and extension of existing methods to invert shear-wave splitting for
358 reservoir fractures (e.g., Verdon et al., 2009; Verdon and Kendall, 2011; Al-Harrasi
359 et al., 2011b; Jones et al., 2014), or resolving the magnitude of the *in situ* differential
360 horizontal stress.

361 6 Conclusion

362 If seafloor microseismic monitoring infrastructure is to be installed for offshore geo-
363 logical CO₂ storage projects, the information gained on the reservoir and surrounding
364 formations should be maximised. We have shown, using analogous data from the
365 permanent reservoir monitoring network at Snorre, that shear-wave splitting can

366 be measured for microseismicity at the field scale using seafloor instrumentation.
 367 Shear-wave splitting has the potential to enable monitoring of the *in situ* azimuth of
 368 maximum horizontal stress at a higher spatial resolution than borehole measurements,
 369 and could be used for monitoring for fluctuations in maximum horizontal stress
 370 azimuth over time. At Snorre, we see that the measured shear-wave splitting fast
 371 polarisations are consistent with the regional maximum horizontal stress azimuth in
 372 the crust of $108 \pm 4^\circ$ with a possible 45° local rotation in maximum horizontal stress
 373 azimuth towards the south of the field. This variation may be due to the depletion
 374 history of the reservoir, similar to results at Valhall.

375 This work demonstrates that shear-wave splitting is a valuable tool for monitoring
 376 spatiotemporal changes in maximum horizontal stress azimuth, providing additional
 377 reservoir information at minimal added cost. The primary requirement is that the
 378 measurement of shear-wave splitting and the likely sources of microseismicity should
 379 be considered in the design and installation of the monitoring network. With further
 380 research to link geomechanical models and the geophysical observations it may also
 381 be possible to use shear-wave splitting to constrain the magnitude of differential
 382 horizontal stress, further increasing the value of shear-wave splitting as a tool to
 383 monitor *in situ* stress for offshore CO₂ storage projects.

384 **7 Acknowledgements**

385 This work was conducted as part of the “Stress history and reservoir pressure for
 386 improved quantification of CO₂ storage containment risks” (SHARP Storage) project,
 387 a collaboration between 16 research institutions and commercial companies in Norway,
 388 UK, the Netherlands, Denmark, and India under the Accelerating CCS Technologies
 389 (ACT3) Programme. The SHARP project has been subsidized through ACT (EC
 390 Project no. 691712), by RCN and Gassnova (Norway), ROV (The Netherlands),
 391 DST (India), BEIS (UK) and EUDP (Denmark). We are grateful to Equinor ASA
 392 and license partners on Snorre (Harbour Energy Norge AS, INPEX Idemitsu Norge
 393 AS, Petoro AS, and Vår Energi ASA), for providing us with permanent reservoir
 394 monitoring system (PRM) data for the 21 March 2022 Tampen Spur event and
 395 its subsequent aftershocks. The views and opinions expressed in this research are
 396 those of the authors and are not necessarily shared by the license partners. TK was
 397 also supported by the University of Oxford’s Strategic Research Fund, through the
 398 Oxford Net Zero programme.

The authors thank Eirik Tvedt, Zoya Zarifi, Brian Baptie, Dan Roberts and members of the SHARP project for discussions, suggestions and feedback which have improved and framed this work. We also thank the reviewers for their constructive feedback on this manuscript.

Part of this research was funded by Natural Environment Research Council (NERC) [NE/W004976/1] as a part of Agile initiative program at the Oxford Martin School.

8 Data Availability

The stress data used here is taken from the World Stress Map (Heidbach et al., 2025) and is publicly available. Earthquake detections and locations used here were first published by (Jenkins et al., 2024) with picks being taken from the Norwegian National Seismic Network bulletin (Norwegian National Seismic Network (NNSN), 2025). The offshore waveform data from was provided to us by Equinor, and the data are not openly accessible to the public. Figures were created using PyGMT (Uieda et al., 2021) and matplotlib (Hunter, 2007). Preprocessing of waveform data was done using routines in Obspy (Beyreuther et al., 2010).

References

- Asplet, J, M Felgett, R Luckett, J Kendall, and D Kühn (2024). “Seismic anisotropy as a measure of in-situ stress for safe CO₂ storage”. In: *85th EAGE Annual Conference & Exhibition*. Vol. 2024. 1. European Association of Geoscientists & Engineers, pp. 1–5. DOI: <https://doi.org/10.3997/2214-4609.2024101469>.
- Asplet, Joseph, Mark Felgett, Tom Kettlety, and John-Michael Kendall (2025). “Passive Monitoring of *in situ* Stress Using Shear-Wave Splitting: Applications to CO₂ Storage and Beyond [Manuscript in review]”. In: *Geological Society, London, Special Publications*. preprint available on EarthArXiv. DOI: <https://doi.org/10.31223/X5WT8S>.
- Backus, George E. (1962). “Long-wave elastic anisotropy produced by horizontal layering”. In: *Journal of Geophysical Research* 67.11, pp. 4427–4440. ISSN: 0148-0227. DOI: <https://doi.org/10.1029/jz067i011p04427>.
- Baird, Alan F., J.-Michael Kendall, James P. Verdon, Andreas Wuestefeld, Todd E. Noble, Yongyi Li, Martin Dutko, and Quentin J. Fisher (2013). “Monitoring increases in fracture connectivity during hydraulic stimulations from temporal variations in shear wave splitting polarization”. In: *Geophysical Journal International* 195.2, pp. 1120–1131. ISSN: 0956-540X. DOI: <https://doi.org/10.1093/gji/ggt274>.

432 Bauer, Robert A., Robert Will, George El-Kaseeh, Paul Jaques, Sallie Greenberg, and Michael
433 Carney (2022). “Microseismic Monitoring, Event Location, and Focal Mechanisms at the Illinois
434 Basin–Decatur Project, Decatur, Illinois, USA”. In: *Geophysical Monitoring for Geologic Carbon*
435 *Storage*. American Geophysical Union (AGU). Chap. 19, pp. 321–341. ISBN: 9781119156871. DOI:
436 <https://doi.org/10.1002/9781119156871.ch19>.

437 Beyreuther, M., R. Barsch, L. Krischer, T. Megies, Y. Behr, and J. Wassermann (2010). “ObsPy:
438 A Python Toolbox for Seismology”. In: *Seismological Research Letters* 81.3, pp. 530–533. DOI:
439 [10.1785/gssrl.81.3.530](https://doi.org/10.1785/gssrl.81.3.530).

440 Booth, David C and Stuart Crampin (1985). “Shear-wave polarizations on a curved wavefront at
441 an isotropic free surface”. In: *Geophysical Journal International* 83.1, pp. 31–45. DOI: <https://doi.org/10.1111/j.1365-246X.1985.tb05154.x>.

443 Cesca, Simone, Francesco Grigoli, Sebastian Heimann, Álvaro González, Elisa Bufo, Samira
444 Maghsoudi, Estefania Blanch, and Torsten Dahm (2014). “The 2013 September–October seismic
445 sequence offshore Spain: a case of seismicity triggered by gas injection?” In: *Geophysical Journal*
446 *International* 198.2, pp. 941–953. ISSN: 0956-540X. DOI: <https://doi.org/10.1093/gji/ggu172>.

448 Chambers, K, JM Kendall, and O Barkved (2010). “Investigation of induced microseismicity at
449 Valhall using the Life of Field Seismic array”. In: *The Leading Edge* 29.3, pp. 290–295. DOI:
450 <https://doi.org/10.1190/1.3353725>.

451 Collins, John A., Cecily J. Wolfe, and Gabi Laske (2012). “Shear wave splitting at the Hawaiian hot
452 spot from the PLUME land and ocean bottom seismometer deployments”. en. In: *Geochemistry,*
453 *Geophysics, Geosystems* 13.2. eprint: <https://agupubs.onlinelibrary.wiley.com/doi/pdf/10.1029/2011GC003881>.
454 ISSN: 1525-2027. DOI: <https://doi.org/10.1029/2011GC003881>.

455 Crampin, Stuart (1987). “Geological and industrial implications of extensive-dilatancy anisotropy”.
456 In: *Nature* 328.6130, pp. 491–496. ISSN: 0028-0836. DOI: <https://doi.org/10.1038/328491a0>.

457 De Meersman, K, J-M Kendall, and M Van der Baan (2009). “The 1998 Valhall microseismic data
458 set: An integrated study of relocated sources, seismic multiplets, and S-wave splitting”. In:
459 *Geophysics* 74.5, B183–B195. DOI: <https://doi.org/10.1190/1.3205028>.

460 Furre, A-K, R Meneguolo, Philip Ringrose, and S Kassold (2019). “Building confidence in CCS:
461 from sleipner to the northern lights project”. In: *First Break* 37.7, pp. 81–87. DOI: <https://doi.org/10.3997/1365-2397.n0038>.

463 Gerst, Alexander and Martha K. Savage (2004). “Seismic Anisotropy Beneath Ruapehu Volcano:
464 A Possible Eruption Forecasting Tool”. In: *Science* 306.5701, pp. 1543–1547. DOI: <https://doi.org/10.1126/science.1103445>.

466 Guzman, Veronica, Aibing Li, and Alexandros Savvaidis (2022). “Stress Variations in the Delaware
467 Basin from Shear-Wave Splitting Analysis”. In: *Seismological Research Letters* 93.6, pp. 3433–
468 3443. ISSN: 0895-0695. DOI: <https://doi.org/10.1785/0220220118>.

469 Hall, Stephen A. and J-Michael Kendall (2003). “Fracture characterization at Valhall: Application
470 of P-wave amplitude variation with offset and azimuth (AVOA) analysis to a 3D ocean-bottom
471 data set”. In: *Geophysics* 68.4, pp. 1150–1160. ISSN: 0016-8033. DOI: <https://doi.org/10.1190/1.1598107>.

- 473 Harmon, Nicholas, Donald W. Forsyth, Karen M. Fischer, and Spahr C. Webb (2004). “Variations in
474 shear-wave splitting in young Pacific seafloor”. en. In: *Geophysical Research Letters* 31.15. eprint:
475 <https://agupubs.onlinelibrary.wiley.com/doi/pdf/10.1029/2004GL020495>. ISSN: 1944-8007. DOI:
476 <https://doi.org/10.1029/2004GL020495>.
- 477 Al-Harrasi, O. H., A. Al-Anboori, A. Wüstefeld, and J.-M. Kendall (2011a). “Seismic anisotropy in
478 a hydrocarbon field estimated from microseismic data”. en. In: *Geophysical Prospecting* 59.2.
479 Publisher: European Association of Geoscientists & Engineers, pp. 227–243. ISSN: 1365-2478.
480 DOI: <https://doi.org/10.1111/j.1365-2478.2010.00915.x>.
- 481 Al-Harrasi, O. H., J.-M. Kendall, and M. Chapman (2011b). “Fracture characterization using
482 frequency-dependent shear wave anisotropy analysis of microseismic data”. In: *Geophysical*
483 *Journal International* 185.2, pp. 1059–1070. ISSN: 1365-246X. DOI: [https://doi.org/10.1111/](https://doi.org/10.1111/j.1365-246x.2011.04997.x)
484 [j.1365-246x.2011.04997.x](https://doi.org/10.1111/j.1365-246x.2011.04997.x).
- 485 Harvey, Stephen, Simon O’Brien, Sara Minisini, Steve Oates, and Mohammed Braim (2021). “Quest
486 CCS facility: Microseismic system monitoring and observations”. In: *Proceedings of the 15th*
487 *greenhouse gas control technologies conference*, pp. 15–18. DOI: [https://dx.doi.org/10.2139/](https://dx.doi.org/10.2139/ssrn.3817042)
488 [ssrn.3817042](https://dx.doi.org/10.2139/ssrn.3817042).
- 489 Hatchell, PJ, PB Wills, and C Didraga (2009). “Production induced effects on near-surface wave
490 velocities at Valhall”. In: *71st EAGE Conference and Exhibition incorporating SPE EUROPEC*
491 *2009*. European Association of Geoscientists & Engineers, cp-127. DOI: [https://doi.org/10.](https://doi.org/10.3997/2214-4609.201400331)
492 [3997/2214-4609.201400331](https://doi.org/10.3997/2214-4609.201400331).
- 493 Heidbach, O, Andreas Barth, Birgit Müller, John Reinecker, Ove Stephansson, Mark Tingay, and
494 A Zang (2016). “WSM quality ranking scheme, database description and analysis guidelines
495 for stress indicator”. In: *World Stress Map Technical Report 16-01*. DOI: [https://doi.org/10.](https://doi.org/10.26443/seismica.v4i1.1101)
496 [26443/seismica.v4i1.1101](https://doi.org/10.26443/seismica.v4i1.1101).
- 497 Heidbach, Oliver et al. (2025). *World Stress Map Database Release 2025*. dataset. GFZ Data
498 Services. DOI: [10.5880/WSM.2025.001](https://doi.org/10.5880/WSM.2025.001).
- 499 Herwanger, Jorg V. and Steve A. Horne (2009). “Linking reservoir geomechanics and time-lapse seis-
500 mics: Predicting anisotropic velocity changes and seismic attributes”. In: *Geophysics* 74.4. eprint:
501 https://pubs.geoscienceworld.org/seg/geophysics/article-pdf/74/4/W13/3220771/gsgpy_74.4_W13.pdf,
502 W13–W33. ISSN: 0016-8033. DOI: <https://doi.org/10.1190/1.3122407>.
- 503 Hudson, Thomas Samuel, Tom Kettlety, John-Michael Kendall, Tom O’Toole, Andrew Jupe, Robin
504 K. Shail, and Augusta Grand (2024). “Seismic Node Arrays for Enhanced Understanding and
505 Monitoring of Geothermal Systems”. In: *The Seismic Record* 4.3, pp. 161–171. ISSN: 2694-4006.
506 DOI: <https://doi.org/10.1785/0320240019>.
- 507 Hunter, J. D. (2007). “Matplotlib: A 2D graphics environment”. In: *Computing in Science &*
508 *Engineering* 9.3, pp. 90–95. DOI: [10.1109/MCSE.2007.55](https://doi.org/10.1109/MCSE.2007.55).
- 509 Igonin, Nadine, James P. Verdon, and David W. Eaton (2022). “Seismic Anisotropy Reveals Stress
510 Changes around a Fault as It Is Activated by Hydraulic Fracturing”. In: *Seismological Research*
511 *Letters* 93.3, pp. 1737–1752. ISSN: 0895-0695. DOI: <https://doi.org/10.1785/0220210282>.
- 512 Jerkins, Annie E., Volker Oye, Celso Alvizuri, Felix Halpaap, and Tormod Kværna (2024). “The
513 21 March 2022 Mw 5.1 Tampen Spur Earthquake, North Sea: Location, Moment Tensor, and

Context". en. In: *Bulletin of the Seismological Society of America* 114.2, pp. 741–757. ISSN: 0037-1106, 1943-3573. DOI: <https://doi.org/10.1785/0120230163>.

Jones, G.a., J.-M. Kendall, I. Bastow, D.g. Raymer, and A. Wuestefeld (2014). "Characterization of fractures and faults: a multi-component passive microseismic study from the Ekofisk reservoir". en. In: *Geophysical Prospecting* 62.4. eprint: <https://onlinelibrary.wiley.com/doi/pdf/10.1111/1365-2478.12139>, pp. 779–796. ISSN: 1365-2478. DOI: <https://doi.org/10.1111/j.1365-2478.2010.00891.x>.

Kendall, J.-M. et al. (2007). "Seismic anisotropy as an indicator of reservoir quality in siliciclastic rocks". In: *Structurally Complex Reservoirs*. Ed. by S. J. Jolley, D. Barr, J. J. Walsh, and R. J. Knipe. Vol. 292. Geological Society of London, pp. 123–136. ISBN: 978-1-86239-241-0. DOI: <https://doi.org/10.1144/SP292.7>.

Kendall, Michael, Toshiko Terakawa, Martha Savage, Tom Kettlety, Daniel Minifie, Haruhisa Nakamichi, and Andreas Wuestefeld (2025). "Changes in seismic anisotropy at Ontake volcano: a tale of two eruptions". In: *Seismica* 4.1. DOI: <https://doi.org/10.26443/seismica.v4i1.1101>.

Keranen, Katie M. and Matthew Weingarten (2018). "Induced Seismicity". en. In: *Annual Review of Earth and Planetary Sciences* 46. Volume 46, 2018. Publisher: Annual Reviews, pp. 149–174. ISSN: 0084-6597, 1545-4495. DOI: <https://doi.org/10.1146/annurev-earth-082517-010054>.

Kettlety, T., D. Kühn, A. Jerkins, E. Martuganova, J. Schweitzer, C. Weemstra, B. Baptie, T. Dahl-Jensen, and P. Voss (2025). *North Sea bulletin and catalogue*. ISC Seismological Dataset Repository. DOI: [10.31905/5NSS060C](https://doi.org/10.31905/5NSS060C).

Kettlety, Tom et al. (2024). "A Unified Earthquake Catalogue for the North Sea to Derisk European CCS Operations". en. In: *First Break* 42.5, pp. 31–36. ISSN: 0263-5046, 1365-2397. DOI: <https://doi.org/10.3997/1365-2397.fb2024036>.

Kühn, D. et al. (2025). "Harmonising seismic bulletins around the North Sea: improving natural seismicity characterisation for CO2 storage preparedness [Manuscript in preperation]". In: *Geoenergy*.

Mordret, Aurélien, Nikolai M. Shapiro, Satish Singh, Philippe Roux, Jean-Paul Montagner, and Olav. I. Barkved (2013). "Azimuthal anisotropy at Valhall: The Helmholtz equation approach". en. In: *Geophysical Research Letters* 40.11. eprint: <https://agupubs.onlinelibrary.wiley.com/doi/pdf/10.1002/grl.50447>, pp. 2636–2641. ISSN: 1944-8007. DOI: <https://doi.org/10.1002/grl.50447>.

Norwegian National Seismic Network (NNSN) (2025). *Earthquake Bulletin Data*. Accessed: 2025-07-25.

Nur, Amos and Gene Simmons (1969). "Stress-induced velocity anisotropy in rock: An experimental study". en. In: *Journal of Geophysical Research* 74.27, pp. 6667–6674. ISSN: 01480227. DOI: <https://doi.org/10.1029/JB074i027p06667>.

Nuttli, Otto (1961). "The effect of the Earth's surface on the S wave particle motion". In: *Bulletin of the Seismological Society of America* 51.2, pp. 237–246. DOI: <https://doi.org/10.1785/BSSA0510020237>.

Ottmøller, Lars, Jan Michalek, Jon-Magnus Christensen, Ulf Baadshaug, Felix Halpaap, Øyvind Natvik, Tormod Kværna, and Volker Oye (2021). "UiB-NORSAR EIDA Node: Integration of

Seismological Data in Norway”. In: *Seismological Research Letters* 92.3, pp. 1491–1500. ISSN: 0895-0695. DOI: <https://doi.org/10.1785/0220200369>.

Pastori, M., P. Baccheschi, and L. Margheriti (2019). “Shear Wave Splitting Evidence and Relations With Stress Field and Major Faults From the “Amatrice-Visso-Norcia Seismic Sequence””. en. In: *Tectonics* 38.9, pp. 3351–3372. ISSN: 0278-7407, 1944-9194. DOI: <https://doi.org/10.1029/2018TC005478>.

Savage, Martha K, Takao Ohminato, Yosuke Aoki, Hiroshi Tsuji, and Sonja M Greve (2010). “Stress magnitude and its temporal variation at Mt. Asama Volcano, Japan, from seismic anisotropy and GPS”. In: *Earth and Planetary Science Letters* 290.3-4, pp. 403–414. DOI: <https://doi.org/10.1016/j.epsl.2009.12.037>.

Scholz, John-Robert, Guilhem Barruol, Fabrice R. Fontaine, Alessandro Mazzullo, Jean-Paul Montagner, Eléonore Stutzmann, Laurent Michon, and Karin Sigloch (2018). “SKS splitting in the Western Indian Ocean from land and seafloor seismometers: Plume, plate and ridge signatures”. In: *Earth and Planetary Science Letters* 498, pp. 169–184. ISSN: 0012-821X. DOI: <https://doi.org/10.1016/j.epsl.2018.06.033>.

Silver, Paul G. and W. Winston Chan (1991). “Shear wave splitting and subcontinental mantle deformation”. In: *Journal of Geophysical Research* 96.B10, p. 16429. ISSN: 0148-0227. DOI: <https://doi.org/10.1029/91JB00899>.

Skurtveit, Elin et al. (2022). “Improved quantification of CO2 storage containment risks — an overview of the SHARP Storage project”. In: *16th Greenhouse Gas Control Technologies Conference 2022 (GHGT-16)*. 16th International Conference on Greenhouse Gas Control Technologies, Lyon, France, 23–27 Oct 2022. SSRN – Social Science Research Network.

Stork, Anna L., James P. Verdon, and J.-Michael Kendall (2015). “The microseismic response at the In Salah Carbon Capture and Storage (CCS) site”. In: *International Journal of Greenhouse Gas Control* 32, pp. 159–171. ISSN: 1750-5836. DOI: <https://doi.org/10.1016/j.ijggc.2014.11.014>.

Teanby, N., J.-M. Kendall, R. H. Jones, and O. Barkved (2004a). “Stress-induced temporal variations in seismic anisotropy observed in microseismic data”. In: *Geophysical Journal International* 156.3. eprint: <https://academic.oup.com/gji/article-pdf/156/3/459/5883127/156-3-459.pdf>, pp. 459–466. ISSN: 0956-540X. DOI: <https://doi.org/10.1111/j.1365-246X.2004.02212.x>.

Teanby, Nicholas A, J-M Kendall, and M Van der Baan (2004b). “Automation of shear-wave splitting measurements using cluster analysis”. In: *Bulletin of the Seismological Society of America* 94.2, pp. 453–463. DOI: <https://doi.org/10.1785/0120030123>.

Thompson, M, M Andersen, RM Elde, SS Roy, and SM Skogland (2015). “Delivering permanent reservoir monitoring for Snorre and Grane”. In: *Third EAGE Workshop on Permanent Reservoir Monitoring 2015*. Vol. 2015. 1. European Association of Geoscientists & Engineers, pp. 1–5. DOI: <https://doi.org/10.3997/2214-4609.201411980>.

Uchida, Naoki, Junichi Nakajima, Kelin Wang, Ryota Takagi, Keisuke Yoshida, Takashi Nakayama, Ryota Hino, Tomomi Okada, and Youichi Asano (2020). “Stagnant forearc mantle wedge inferred from mapping of shear-wave anisotropy using S-net seafloor seismometers”. en. In:

595 *Nature Communications* 11.1. Publisher: Nature Publishing Group, p. 5676. ISSN: 2041-1723.
 596 DOI: [10.1038/s41467-020-19541-y](https://doi.org/10.1038/s41467-020-19541-y).

597 Uieda, Leonardo, Dongdong Tian, Wei Ji Leong, Liam Toney, Michael Grund, Jack T. Williams,
 598 Megan Jones, William Schlitzer, Jonas de Souza, and Paul Wessel (2021). “PyGMT: A Python
 599 interface for the Generic Mapping Tools”. In: *The Journal of Open Source Software* 6.64, p. 3488.
 600 DOI: [10.21105/joss.03488](https://doi.org/10.21105/joss.03488).

601 Verdon, J. P., J.-M. Kendall, and Andreas Wüstefeld (2009). “Imaging fractures and sedimentary
 602 fabrics using shear wave splitting measurements made on passive seismic data”. In: *Geophysical
 603 Journal International* 179.2. Publisher: Blackwell Publishing Ltd Oxford, UK, pp. 1245–1254.
 604 DOI: <https://doi.org/10.1111/j.1365-246X.2009.04347.x>.

605 Verdon, James P and J-Michael Kendall (2011). “Detection of multiple fracture sets using observa-
 606 tions of shear-wave splitting in microseismic data”. In: *Geophysical Prospecting* 59.4, pp. 593–608.
 607 DOI: <https://doi.org/10.1111/j.1365-2478.2010.00943.x>.

608 Walsh, E., R. Arnold, and M. K. Savage (2013). “Silver and Chan revisited”. In: *Journal of
 609 Geophysical Research: Solid Earth* 118.10, pp. 5500–5515. ISSN: 21699313. DOI: [https://doi.
 610 org/10.1002/jgrb.50386](https://doi.org/10.1002/jgrb.50386).

611 Wuestefeld, Andreas, Othman Al-Harrasi, James P Verdon, James Wookey, and J Michael Kendall
 612 (2010). “A strategy for automated analysis of passive microseismic data to image seismic
 613 anisotropy and fracture characteristics”. In: *Geophysical Prospecting* 58.5, pp. 755–773.

614 Zatsepin, Sergei V. and Stuart Crampin (1997). “Modelling the compliance of crustal rock—I.
 615 Response of shear-wave splitting to differential stress”. In: *Geophysical Journal International*
 616 129.3, pp. 477–494. ISSN: 1365-246X. DOI: [https://doi.org/10.1111/j.1365-246x.1997.
 617 tb04488.x](https://doi.org/10.1111/j.1365-246x.1997.tb04488.x).

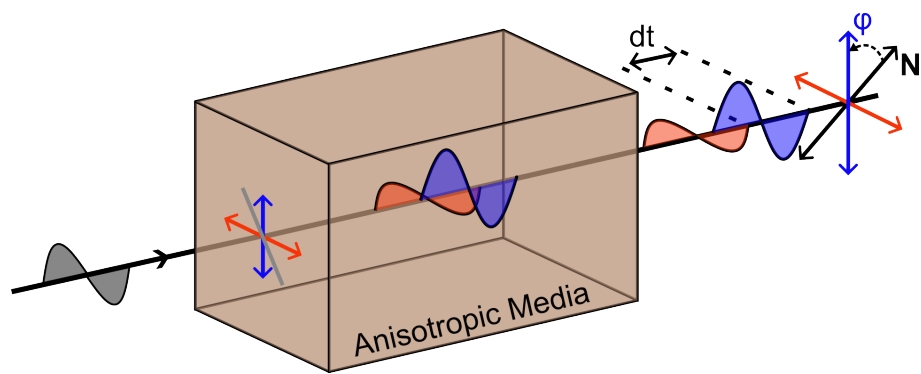


Figure 1: Schematic cartoon illustrating shear-wave splitting.

Record Section for M_L 0.7 aftershock
Origin time: 2022-03-21 05:43:02

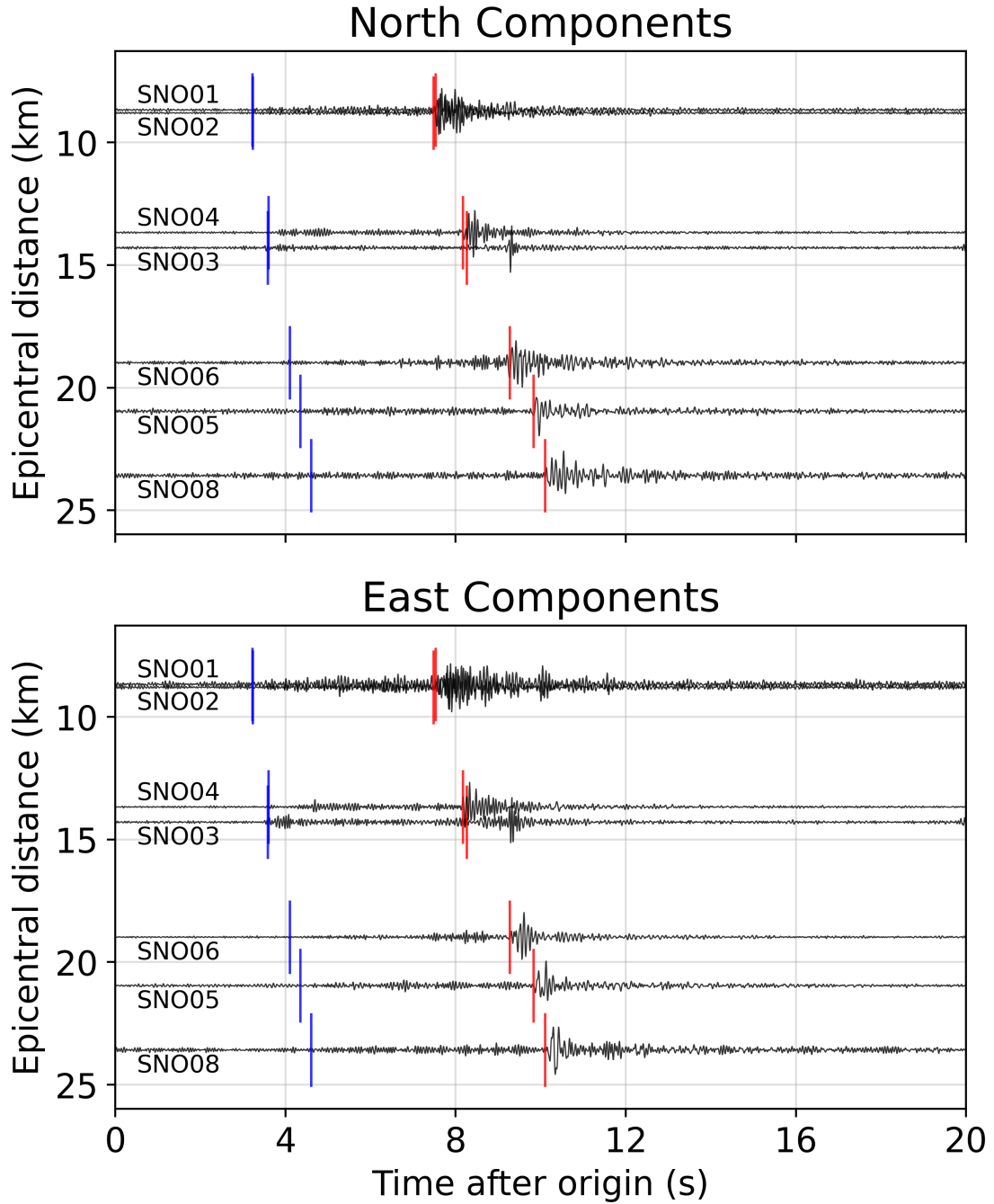


Figure 2: Horizontal component seismograms recorded by permanent reservoir monitoring stations for a M_L 0.7 aftershock of the M_W 21st March 2022 Tampen Spur earthquake. Blue and red bars show the P and S arrival times reported in the NNSN bulletin (Norwegian National Seismic Network (NNSN), 2025). Only data for PRM sensors within the shear-wave window of the event are shown.

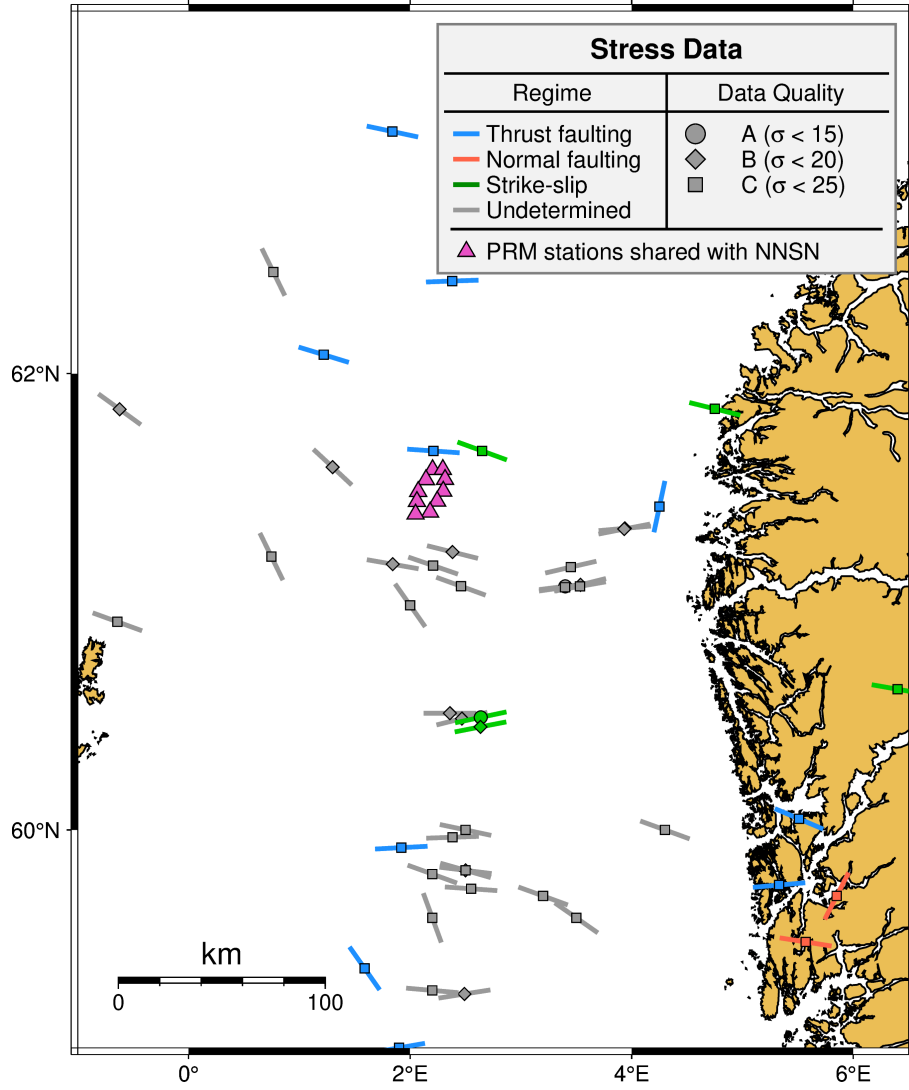


Figure 3: Map showing borehole stress data from the World Stress Map database (Heidbach et al., 2025). Bars show the interpreted S_{Hmax} orientation and symbols correspond to data quality where A (circle) has an uncertainty in S_{Hmax} orientation of $< 15^\circ$, B (diamond) has an uncertainty of $< 20^\circ$ and C has an uncertainty $< 25^\circ$. Grey triangles show the location of Snorre PRM stations that share data with the NNSN.

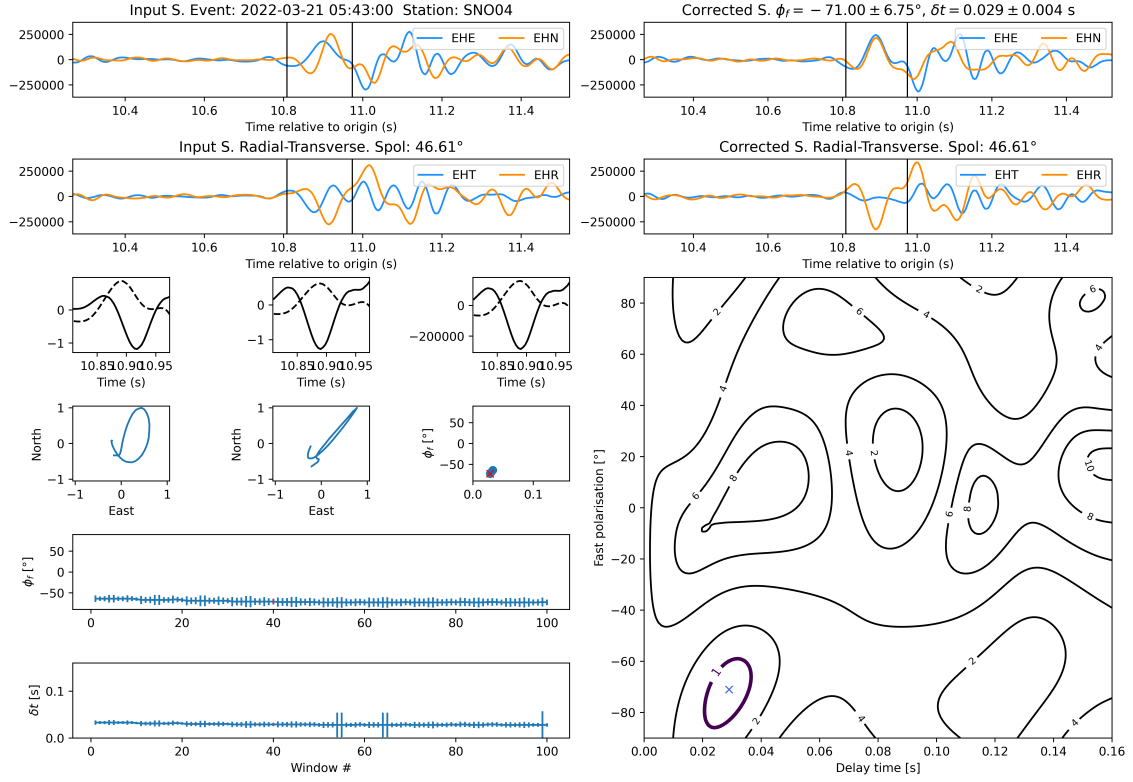


Figure 4: Example shear-wave splitting measurement made at for a M_L 0.7 earthquake which occurred at 2022-03-21 05:41:43 UTC and was recorded by PRM sensor SNO04 at the Snorre field. After manual inspection this measurement is categorised as an ‘A’ or high quality measurement of shear-wave splitting. Top panels show the input (top left) and corrected (top right) shear-wave phase, where the vertical black bars show the optimum analysis window. The second row shows in the input and corrected waveforms rotated to the measured source polarisation direction. The third row shows the normalised input and corrected waveforms, along with the unnormalised, corrected waveforms. The fourth row shows particle motion plots, which shows the North and East component waveforms plotted against each other, for the input and corrected waveforms, along with the measured fast polarisation (ϕ_f) and delay time (δt) for each window used in the cluster analysis of (Teanby et al., 2004b). Lower panels show ϕ_f and δt plotted against window number. The contour plot on the lower right shows the summarised result of the grid search over $\phi_f, \delta t$ for the optimum analysis window, with contours showing the objective function $\frac{\lambda_2}{\lambda_1}$. Here $\frac{\lambda_2}{\lambda_1}$ has been normalised by the estimated 95% confidence value (Equation 2) with the bold contour enclosing the 95% confidence region. Blue cross shows the best fitting shear-wave splitting parameters.

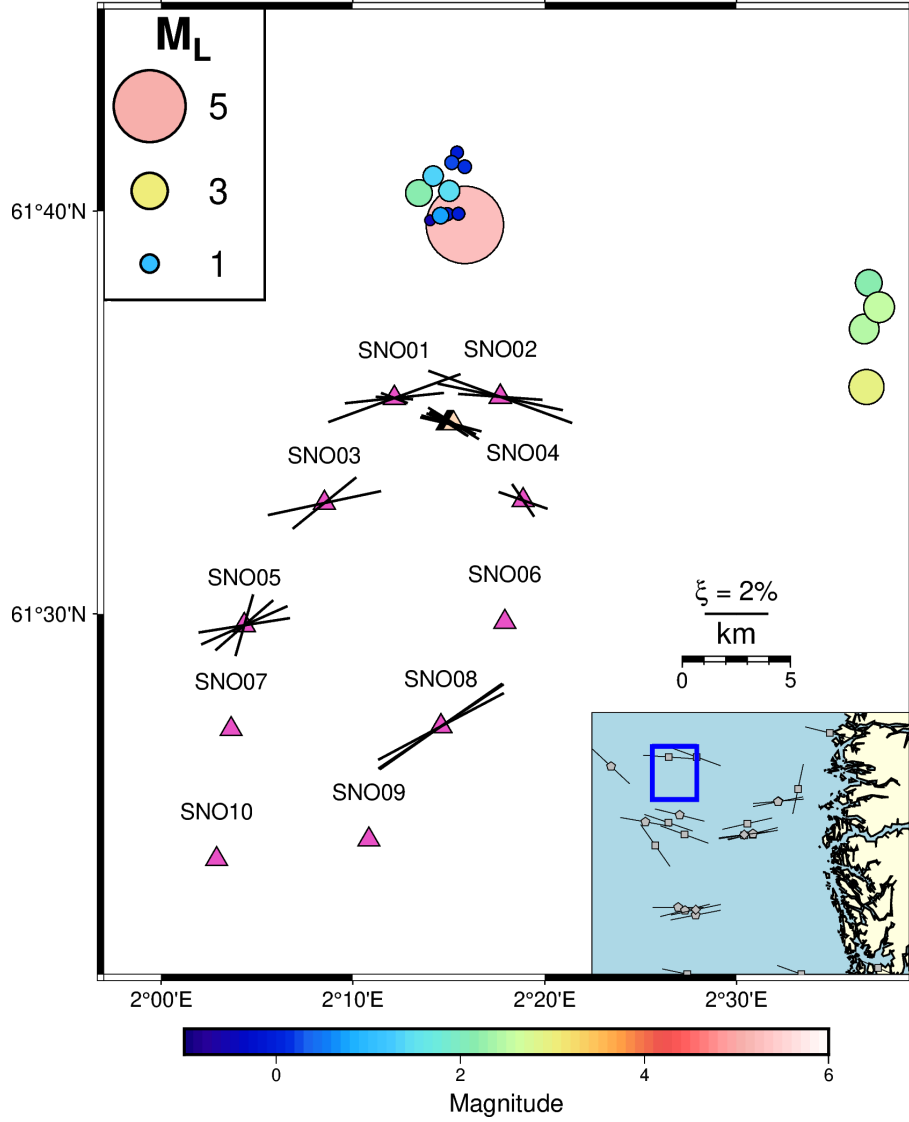


Figure 5: Shear-wave splitting measurements for data from permanent reservoir monitoring (PRM) stations (triangles) at the Snorre field. Shear-wave splitting measurements are shown by the black bars whose orientation corresponds to ϕ and length is proportional to ξ , which is calculated from δt following equation 3 assuming a V_S of 2.8 km s^{-1} and a 5 km thick layer of anisotropy. Earthquakes used (blue circles), the 21st March 2022 M_W 5.1 Tampen Spur earthquake and subsequent aftershocks, are plotted at the locations of Jerkins et al. (2024). Data from 10 PRM stations, which is shared with the Norwegian National Seismic Network (Ottemöller et al., 2021), is used for all earthquakes. For the Tampen Spur mainshock, waveform data from an additional 50 PRM stations was provided by Equinor. Inset map shows borehole stress data taken from the World Stress Map data base (Heidbach et al., 2025), plotted as in Figure 3.

S phase of M_W 5.1 Tampen Spur Mainshock
Recorded by 10 closest PRM stations
Origin time: 2022-03-21 05:32:57

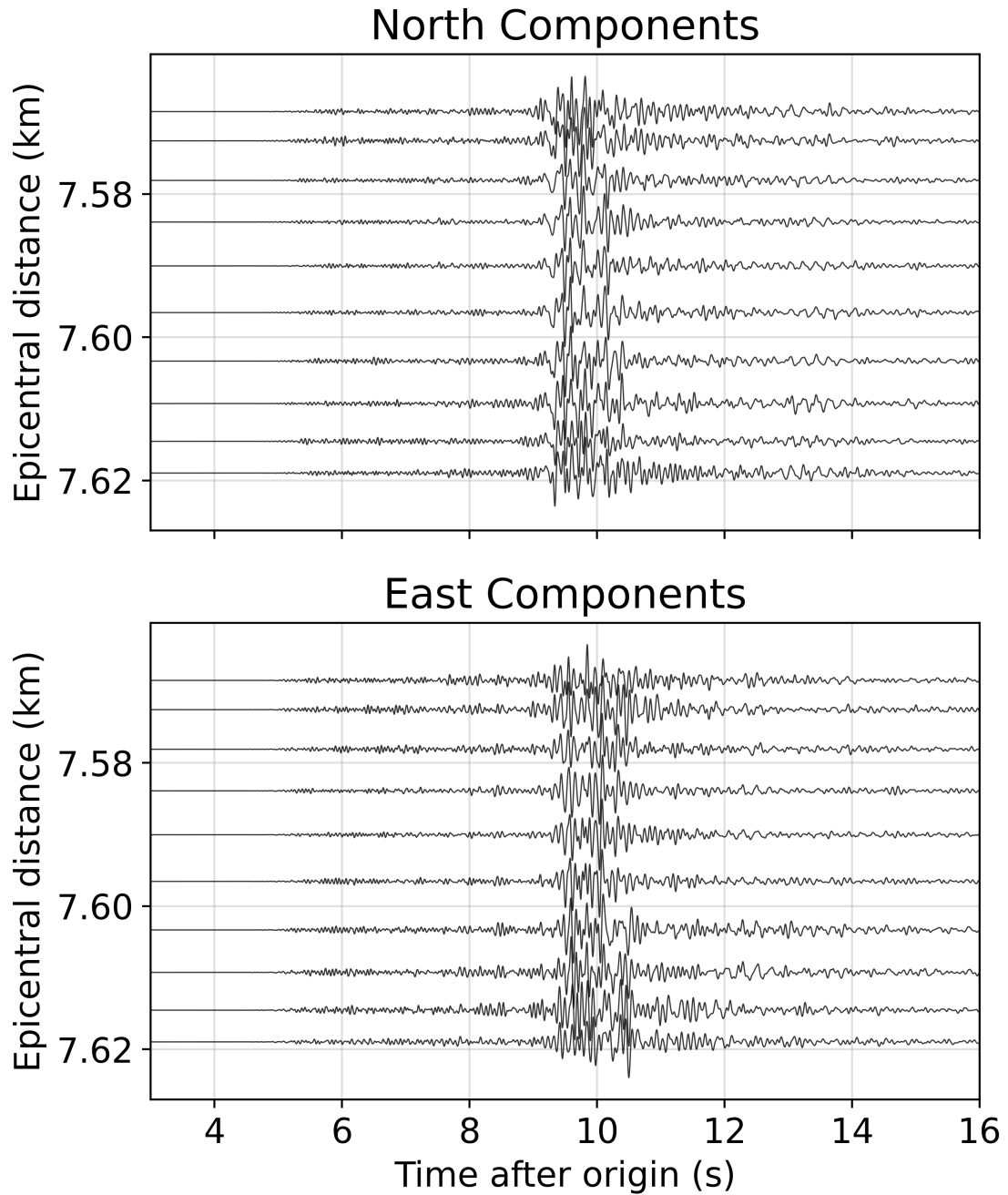


Figure 6: Horizontal component seismograms showing the shear-wave arrivals from the M_W 21st March 2022 Tampen Spur earthquake recorded by the 10 PRM sensors closest to the hypocenter that were available to this study.

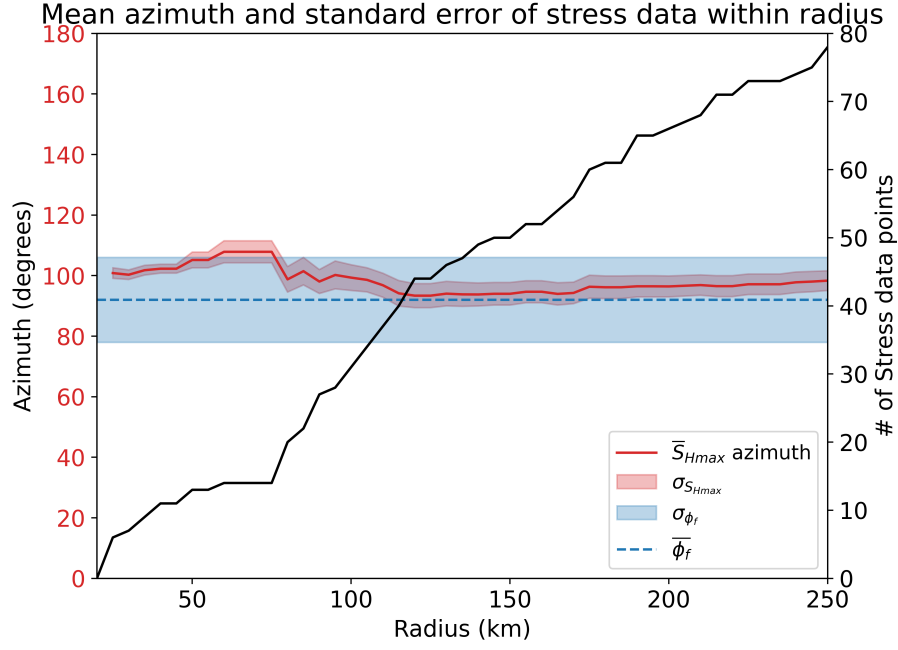


Figure 7: Regional S_{Hmax} azimuth for Snorre (blue line), estimated by taking the circular mean of S_{Hmax} azimuth data within a given radius of the centre of the PRM network, as a function of averaging radius. Shaded region shows the circular standard error. Red line shows the number of datapoints included in the averaging. S_{Hmax} azimuth data is taken from 2025 version of the World Stress Map (Heidbach et al., 2025)

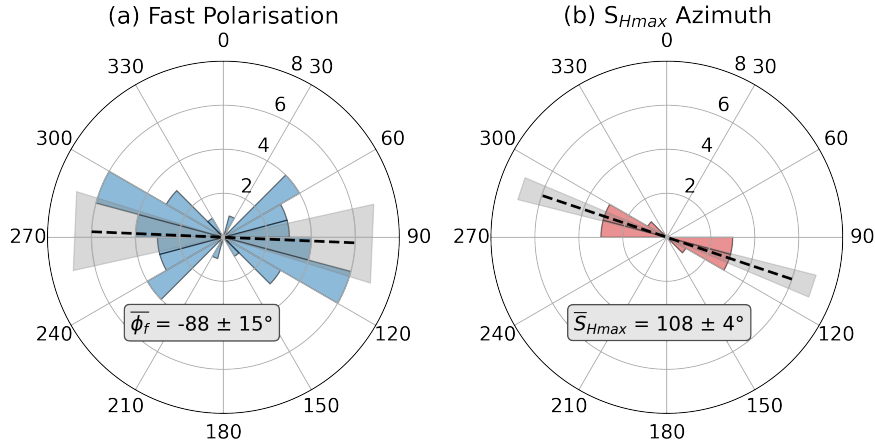


Figure 8: Rose histograms showing the shear-wave splitting fast polarisation data at Snorre (a) and S_{Hmax} azimuth data within 50 km of Snorre (b). The black dashed line indicates the circular mean of each dataset, with the grey shaded region representing the circular standard error. Individual shear-wave splitting measurements can be seen in Figure 5.

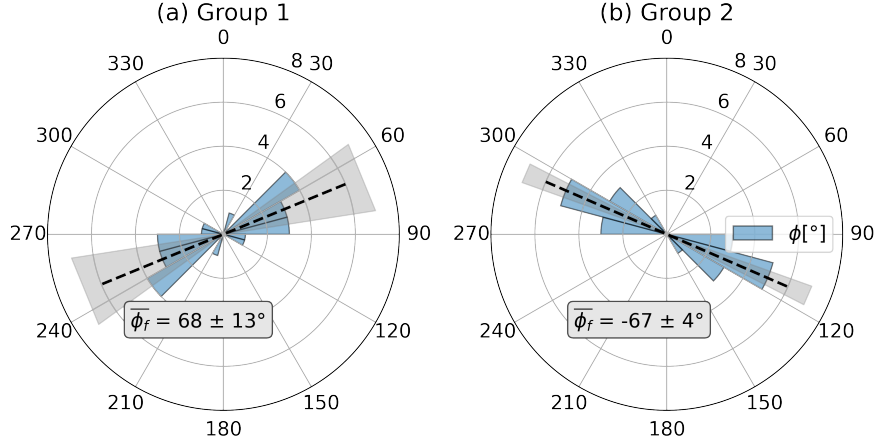


Figure 9: Rose histograms showing the shear-wave splitting fast polarisation data at Snorre recorded by the PRM stations SNO01, SNO03, SNO05 and SNO08 (a) and the remaining eastern stations (b). The black dashed line indicates the circular mean, $\bar{\phi}_f$ of each dataset, with the grey shaded region representing the circular standard error.

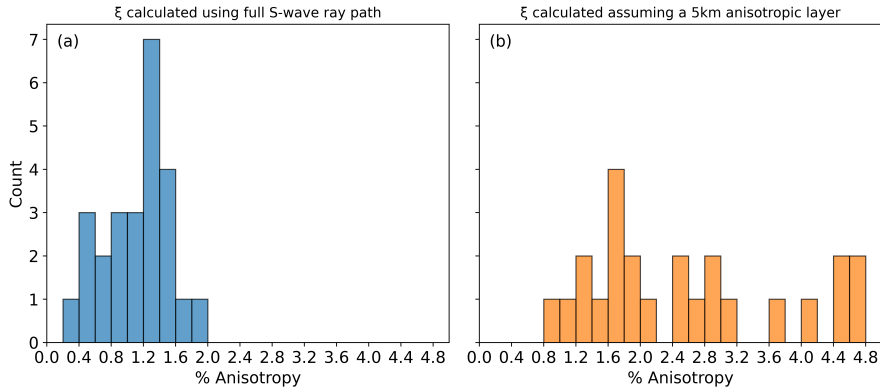


Figure 10: Histograms showing the estimated percentage anisotropy, calculated following equation 3, assuming that anisotropy accumulates along the entire shear-wave ray-path (a) and anisotropy only in the uppermost 5 km of the crust. In (a) we assume a mean V_S of 5.7 km s^{-1} and in (b) we assume a mean V_S of 2.8 km s^{-1} .